**ORIGINAL PAPER**

# Bone toughening through stress-induced non-collagenous protein denaturation

Z. Wang[1,2] · D. Vashishth[2,3] · R. C. Picu[1]

## Abstract

Bone toughness emerges from the interaction of several multiscale toughening mechanisms. Recently, the formation of nanoscale dilatational bands and hence the accumulation of submicron diffuse damage were suggested as an important energy dissipation processes in bone. However, a detailed mechanistic understanding of the effect of this submicron toughening mechanism across multiple scales is lacking. Here, we propose a new three-dimensional ultrastructure volume element model showing the formation of nanoscale dilatational bands based on stress-induced non-collagenous protein denaturation and quantify the total energy released through this mechanism in the vicinity of a propagating crack. Under tensile deformation, large hydrostatic stress develops at the nanoscale as a result of local confinement. This tensile hydrostatic stress supports the denaturation of non-collagenous proteins at organic–inorganic interfaces, which leads to energy dissipation. Our model provides new fundamental understanding of the mechanism of dilatational bands formation and its contribution to bone toughness.

**Keywords** Bone · Mineralized collagen fibril · Finite element modeling · Non-collagenous proteins · Fracture toughness

## 1 Introduction

Bone exhibits a hierarchical organization from the nano- to the macroscale (Rho et al. 1998; Weiner et al. 1999). Its mechanical properties depend on the specific architecture at all levels of the hierarchy (Hamed et al. 2010). It is reported that, due to its heterogeneous structure, bone can withhold moderate damage accumulation without breaking (Vashishth et al. 1997; Zioupos and Currey 1998; Vashishth

✉ D. Vashishth
  vashid@rpi.edu

✉ R. C. Picu
  picuc@rpi.edu

1 Department of Mechanical, Aerospace and Nuclear Engineering, Rensselaer Polytechnic Institute, Troy, NY 12180, USA

2 Center for Biotechnology and Interdisciplinary Studies, Rensselaer Polytechnic Institute, Troy, NY 12180, USA

3 Department of Biomedical Engineering, Rensselaer Polytechnic Institute, Troy, NY 12180, USA

et al. 2000). Macroscopic bone fracture toughness is defined by the synergistic interaction of multiple toughening mechanisms. Many of the microscale toughening mechanisms observed in ceramics and brittle engineering materials, such as crack pinning, crack deflection and crack bridging, have also been discussed in the context of bone (Vashishth et al. 1997; Nalla et al. 2003; Taylor et al. 2007; Zimmermann et al. 2014). Dissipation of energy at submicron- and nanoscales is generally accepted, but a detailed understanding of the nanoscale mechanism of energy dissipation and moreover its effect at the macroscale are still largely unknown.

The nanoscale building unit of bone is the mineralized collagen fibril (MCF) whose structure and mechanical properties have been investigated (Jäger and Fratzl 2000; Gupta et al. 2006; Almer and Stock 2005, 2007; Deshpande and Beniash 2008; Yuan et al. 2010). MCFs are organic/inorganic composites composed of mainly type-I collagen, inorganic mineral platelets and smaller quantities of non-collagenous proteins (NCPs) (De Buffrénil et al. 2004). Collagen triple helices run parallel to the longitudinal direction of MCF forming a staggered structure and self-assemble into relatively soft fibrils with the diameter on the order of 100 nm (Hodge and Petruska 1962). Mineral crystals grow in the gap

zones (intra-fibrillar mineral) and outside the collagen fibrils (extra-fibrillar mineral) mechanically reinforcing the collagen structure (Grynpas et al. 1984; Fratzl et al. 1996). NCPs are known to be important regulators of bone mineralization process (Termine et al. 1981; Boskey et al. 1998; Poundarik et al. 2011).

Importantly, studies suggest that NCPs also play a direct structural role and act as 'glue' at the mineral–organic interface (Fantner et al. 2005; Hamed et al. 2012; Poundarik et al. 2012; Hang et al. 2014). The details of structural function of NCPs are still a matter of debate. Recent studies (Poundarik et al. 2012, 2015) report a 31% macroscopic toughness reduction in NCPs knockout mice femurs. Furthermore, nanoscale damage in the form of dilatational bands (Poundarik et al. 2012; Nikel et al. 2013) was observed in diffuse damage regions of wild-type mice bone but not in the knockouts due to the absence of the relevant NCPs. The dilatational bands have dimensions on the order of $\sim$ 100 nm and align with the collagen fibril (Poundarik et al. 2012). These findings are consistent with past research, indicating that diffuse damage can be viewed as submicron 'cracks' (Schaffler et al. 1995; Burr et al. 1998; Vashishth et al. 2000; Seref-Ferlengez and Basta-Pljakic 2014). Such diffuse damage zone is observed in the process zone of a major crack or the vicinity of microcracks (Vashishth et al. 2000; Poundarik et al. 2012). Such localized inelastic deformation leads to energy dissipation. The energy released during a protein denaturation event was estimated to range from 1.1 to 54.5 eV (Gupta et al. 2006; Poundarik et al. 2012), and it was conjectured, when scaled-up to the macroscopic scale of the sample, the mechanism can lead to significant energy release.

In this study, we develop a mechanistic model of the nanoscale mechanism leading to the formation of dilatational bands in bone. The mechanism is based on the published experimental data indicating co-localization of the inelastic deformation within NCP complexes distributed at mineral–collagen interfaces (Poundarik et al. 2012; Nikel et al. 2013; Stock 2015). Topological confinement of the soft organic phase due to the specific extra-fibrillar mineral arrangement leads to important stress concentration in the region of the gaps between mineral platelets, which produce protein denaturation. This process generates crack-like features, which we refer to as 'denaturation front,' extending along the extra-fibrillar mineral platelet surfaces. The mechanism is quantified using a finite element model of the submicron structure of the MCFs and extra-fibrillar mineral. The model allows the estimation of the energy released at each such site, which, in turn, allows evaluating the energy released via this mechanism in the vicinity of a crack tip.

## 2 Model development

Mineralized collagen fibrils (MCFs) are an organic/inorganic composite material. The unique interactions between the mineral phase, collagen, and NCPs determine their material properties and mechanical function (Deshpande and Beniash 2008; Yuan et al. 2010). In this work, we use a three-dimensional volume element (VE) model with the stochastic arrangement of extra-fibrillar mineral structure to investigate the nanoscale stress and strain distribution.

Microscale computed tomography (micro-CT) measurements indicate that the mineral volume fraction in cortical bone from human and bovine tibia is 37.9%. This value results from our studies (see supplementary information) and is supported by the literature (Ellman et al. 2013; Ciuchi et al. 2013). The intra-fibrillar mineral is located in the gap zone of collagen fibril (Hodge and Petruska 1962). Evidence exists that significant amounts of mineral are extra-fibrillar (Lees and Prostak 1988; Pidaparti et al. 1996; Schwarcz et al. 2014); specifically, only 25–42% of the total mineral can be accommodated by intra-fibrillar gap zones, as predicted by various collagen molecular packing models (Bonar et al. 1985; Alexander et al. 2012; Nair et al. 2014). Also, the extra-fibrillar mineral is thought to be more important for the stiffness and compression strength of bone. Karunaratne et al. (2012) show that the nanoscale modulus of wild-type mice bone increases from 13 to 40 GPa during growth, from 4 weeks to 16 weeks, while the rickets model with incomplete extra-fibrillar mineralization yields apparent modulus from 1 to 6 GPa. Mineralized tendon samples that contain exclusively intra-fibrillar mineral yield apparent modulus of approximately 1 GPa (Landis et al. 1996; Gupta et al. 2004; Meyers et al. 2008; Tresoldi et al. 2013). An atomistic model (Nair et al. 2013) shows that intra-fibril mineral alone, even with 40% mineral density, is not sufficient to explain the load-bearing properties of bone. Therefore, in the current work, we focus on the extra-fibrillar mineral distribution and account for the intra-fibrillar mineral implicitly, by using a homogenized representation for the MCF. We assume that NCPs are localized exclusively in the extra-fibrillar space, at the interface between mineral platelets and matrix (Nikel et al. 2013). The NCPs are not represented explicitly in the model, rather their effect is included in the mechanical properties of these interfaces which are characterized by predefined cohesive energy (Termine et al. 1981; Hamed et al. 2012; Hang et al. 2014).

To generate a model of the ultrastructure of bone, we start from transmission electron microscopy (TEM) observations of fibril bundles (McNally et al. 2012; Schwarcz et al. 2014), showing extra-fibrillar mineral platelets distributed in

a shell-like fashion around MCF. Similar extra-fibrillar mineral structure patterns have been reported by other groups such as (Rubin et al. 2003, Reznikov et al. 2014) who show TEM images of focused ion beam-milled femur bone samples similar to that of McNally et al. (2012). Due to bio-mineralization regulation and topological packing reasons, the mineral platelets are arranged roughly parallel to each other, with their $c$ axis direction oriented approximately parallel to the collagen fibril axis (Jaschouz et al. 2003). The platelet predominant orientation applies to both the intra- and extra-fibrillar minerals. A TEM image from (McNally et al. 2012) representing the arrangement of the extra-fibrillar mineral is reproduced in Fig. 1a. This shows

mineral lamellae arranged parallel to each other and packed in the space between collagen fibrils. Geometric parameters of this arrangement and mean dimensions of individual mineral platelets are obtained from this image and from other literature sources (Jäger and Fratzl 2000; Schwarcz et al. 2014) and are listed in Table 1 and shown in Fig. 1.

Geometries equivalent to that in Fig. 1a were created by starting with a Voronoi tessellation in the $x-y$ plane perpendicular to the direction of the MCFs (Fig. 1b). Seed points are generated in a regular hexagonal pattern, and then, their positions are perturbed by random shifts. The tessellation resulting from this set of seed points contains almost equiaxed cells (Fig. 1b). The intersections of the extra-
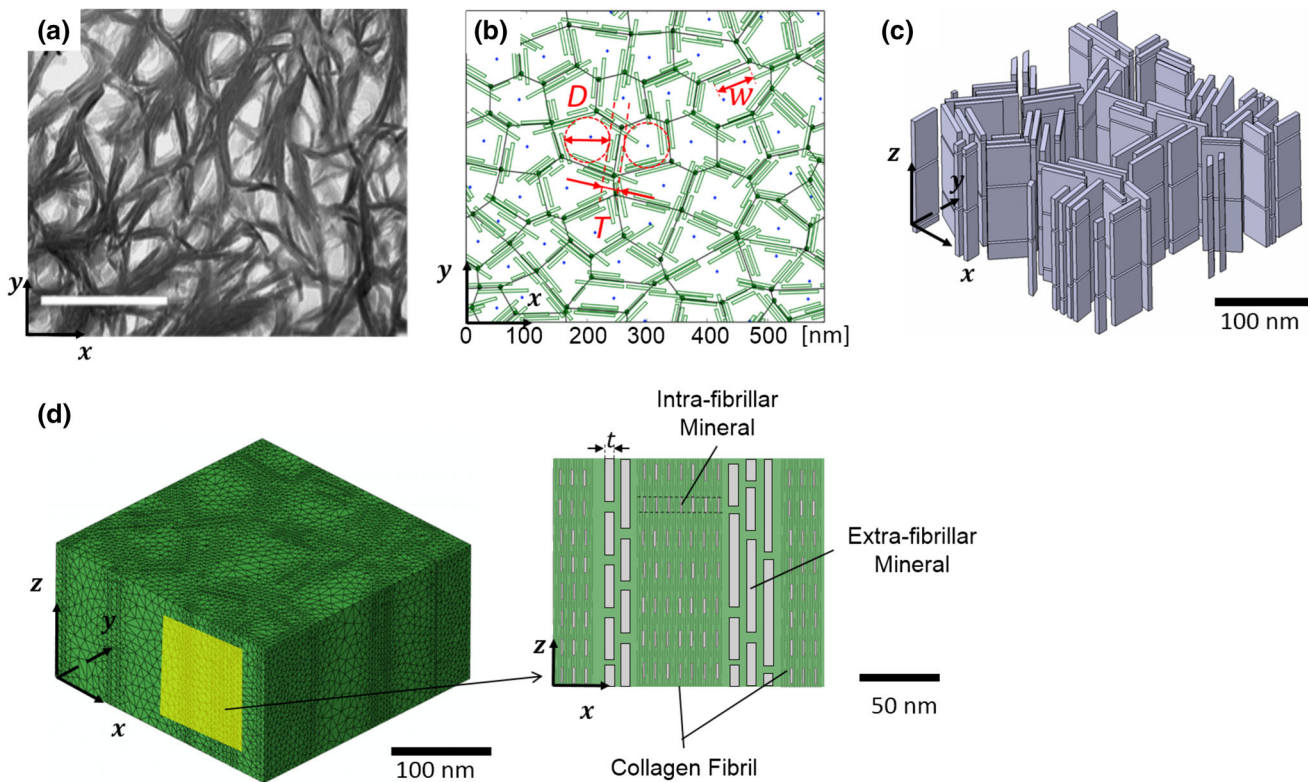


Fig. 1 a Bright-field TEM image of collagen fibrils in the projection parallel to the fibril axis ($z$-direction), reproduced with permission from (McNally et al. 2012), scale bar = 100 nm; b two-dimensional Voronoi representation of mineral arrangement in the $x-y$ plane, perpendicular to the MCF. A generic collagen fibril diameter ($D$), width of an extra-fibrillar mineral ($w$) and extra-fibrillar mineral bundle thickness ($T$) are shown; c three-dimensional mineral platelets and inter-platelet gaps after extruding the configuration in b in the $z$-direction (the direction of the MCF axis); d meshed VE corresponding to the mineral platelet arrangement in c. The structure is referred to a Cartesian coordinate system with the $z$-axis aligned with the longitudinal direction of bone. The inset diagram shows the 2D subscale MCFs schematic diagram not resolved in FEM model with collagen fibril, intra-/extra-fibrillar mineral

Table 1 Constituent dimensions used to construct the model (McNally et al. 2012; Jäger and Fratzl 2000; Schwarcz et al. 2014)

| Measurement type | Value |
| --- | --- |
| Thickness of extra-fibrillar mineral platelet, $t$ | 5 nm |
| Width of extra-fibrillar mineral platelet, $w$ | $68 \pm 18$ nm |
| Average extra-fibrillar mineral bundle thickness, $T$ | $27.7 \pm 10.4$ nm |
| Average of MCF major and minor axes, $\overline{D}$ | $45.4 \pm 22.8$ nm |

fibrillar mineral platelets with the $x-y$ plane are generated parallel to the edges of each Voronoi cell. The $c$-axis of the platelets is in the $z$-direction. The position of mineral platelets along given cell edge is selected at random. The number of platelets per edge is also stochastic, in the range 1–4, in agreement with TEM observations. This procedure leads to geometries such as that shown in Fig. 1b. Further, the mineral plate traces are replaced with actual platelets of thickness $t = 5$ nm and width sampled from a lognormal distribution of mean $w = 68$ nm and standard deviation 18 nm (Table. 1) (McNally et al. 2012; Schwarcz et al. 2014). Here, we assume that all platelets have the same thickness since the reported variation of the thickness is much smaller than the variation of length and width of platelets (Fratzl et al. 1996; Burger et al. 2008; Poundarik et al. 2011). The spacing of platelets in the direction perpendicular to the cell edge is 1 to 3 nm, as suggested in the literature (Gupta et al. 2006; McNally et al. 2012; Schwarcz et al. 2014). The addition of mineral platelets to the model ends once the total mineral volume fraction reaches the imposed volume fraction of 26.6%. Note that the space close to the core of each Voronoi cell is occupied by the MCF. Further details of the procedure are presented in Supplementary information.

To produce the three-dimensional structure of the fibril bundle, the mineral platelets are extruded in the $z$-direction, i.e., the direction of the MCF axis. The length of each mineral platelet is set to 50 nm, and the platelets are staggered in the $z$-direction as shown in Fig. 1c. X-ray diffraction and modeling studies (Jäger and Fratzl 2000; Gupta et al. 2006; Almer and Stock 2007) confirm that the mineral staggered arrangement is important for load transfer in mineralized collagen fibrils. The effect of the deterministic parameter representing the mineral platelet length on the results of this study is presented in supplementary information section.

A CAD model with geometry defined above is developed as shown in Fig. 1c. The model is meshed using the SimModeler suite from Simmetrix Inc. (Li et al. 2005). The interface between MCF and mineral platelets is well bonded, except in regions where protein denaturation occurs. Tetrahedral elements with linear interpolation functions are used throughout. Models have on the order of $6 \times 10^5$ 4-nodes tetrahedral elements and approximately $3 \times 10^5$ degrees of freedom associated with $\sim 1.1 \times 10^5$ nodes. The created FEM model is shown in Fig. 1d. Mesh refinement is used in the gap region between mineral platelets in the $z$-direction.

According to experiments and atomistic simulations (Peroos et al. 2006; Hang and Barber 2011; Nair et al. 2014), both the collagen fibril and the extra-fibrillar mineral behave elastically in the physiological strain range ($10^{-3} \sim 3 \times 10^{-3}$). Therefore, we consider linear elastic behavior for both mineral platelets and matrix material. The mineral platelets are assigned isotropic elastic behavior of modulus 80 GPa and Poisson's ratio 0.28 (Koch et al. 2007; Yuan et al. 2010).

The chosen value for the mineral modulus is based on the observation that the modulus of nanoscale mineral platelets is much smaller than that reported for bulk hydroxyapatite (Yuan et al. 2010). MCF fills the space between groups of extra-fibrillar mineral, i.e., the interior of the Voronoi cells in Fig. 1b and its mechanical properties are considered to be similar to mineralized turkey tendon (Landis et al. 1996; Tresoldi et al. 2013). We denote this as the 'matrix' material and assign a modulus of 1 GPa based on the experimental values (Gupta et al. 2004; Meyers et al. 2008). Poisson's ratio of the matrix material ranges from 0.4 to 0.46 in separate models (Jin and Lewis 2004; Kiviranta et al. 2006). Further, osteocalcin is reported to bind strongly to hydroxyapatite mineral platelets and has the ability to interact with organic matrix through osteopontin and other NCPs (Hauschka and Wians 1989; Ritter et al. 1992). Therefore, as reported (Termine et al. 1981; Hamed et al. 2012; Hang et al. 2014), the NCPs are considered to be located at the mineral–organic interface, as shown in the insets of Fig. 1d. As defined above, the NCPs are subscale features (that are not resolved in the FEM model) and their presence is reflected in the mechanical behavior of the mineral–matrix interface. The interface can be weak if its strength relies entirely on molecular entanglements (Stock 2015). However, when the denaturation of OC–OPN complexes is included, the interface becomes stronger (Poundarik et al. 2012). To account for both weak and strong interfaces, we considered a wide interface energy release rate range from $0.04$ mJ/m$^2$ ($2.5 \times 10^{-4}$ eV/nm$^2$) to $10.91$ mJ/m$^2$ ($0.068$ eV/nm$^2$). These values are reproduced from Gupta et al. (2006) and Poundarik et al. (2012).

The model is constructed to allow the application of periodic boundary conditions in all directions. In the uniaxial loading case, periodic boundary conditions are applied in the $x-z$ and $z-y$ planes and displacements are imposed on faces perpendicular to the $z$-axis such that the sample is loaded in uniaxial tension. Global physiological strain levels range from $10^{-3}$ to $3 \times 10^{-3}$, while strain larger than $3 \times 10^{-3}$ can only be produced during the vigorous activity (Schaffler et al. 1989; Burr et al. 1996). Zero traction boundary conditions are applied in directions perpendicular to the $z$-axis. Situations in which the model is loaded multiaxially are considered in conjunction with dilatational band formation in the vicinity of a major crack tip.

To evaluate the released energy associated with NCP denaturation, we assume that the denaturation always begins at the location of maximum normal stress acting perpendicular to the matrix–mineral interface. A crack-like feature is created along a randomly selected interface in this model at a site where the local stress state reaches a maximum. Any interface in the model can be selected for this purpose since all interfaces carry statistically similar loads, and periodic boundary conditions are applied to the model. The strain energy difference between models with and without mod-
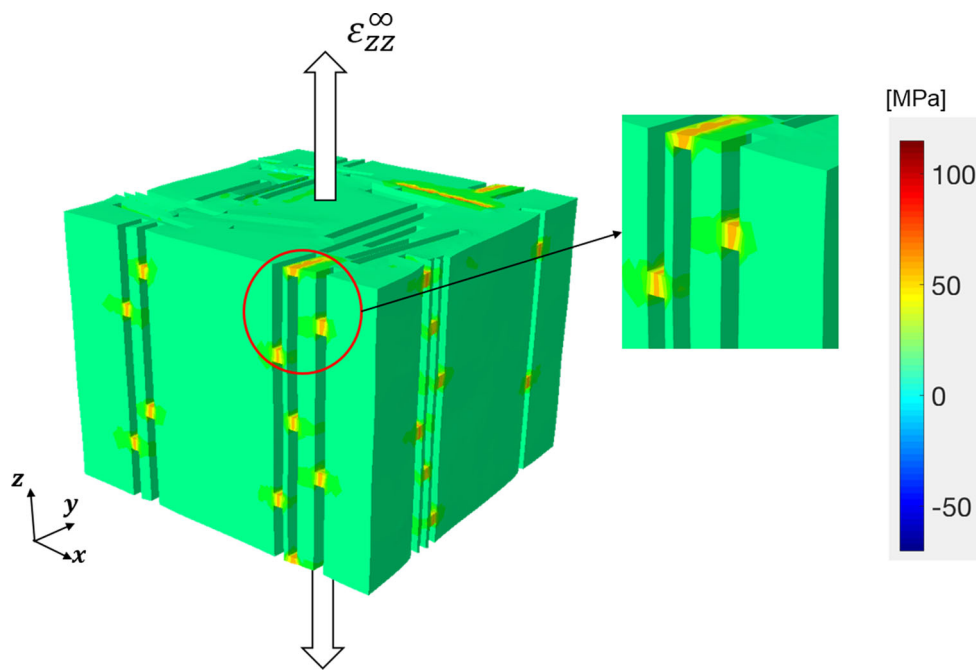
**Fig. 2** Hydrostatic stress distributions in the nanoscale VE subjected to uniaxial tension in the $z$-direction (shown by arrows)

ified interfaces but under the same boundary conditions is computed. The process is repeated in each case for various dimensions of the denatured interfacial region to evaluate the energy released due to the growing interfacial NCP denaturation front.

# 3 Results and discussion

## 3.1 Stress distribution in the undamaged sample

The large elastic heterogeneity and the complexity of the geometrical arrangement lead to rather large spatial stress variability. Of interest are the local stresses at interfaces and, in particular, the normal tensile stress acting in the direction perpendicular to these interfaces. At this stage of the investigation, it is considered that the far-field strain $\varepsilon_{zz}^\infty$ is tensile and acts parallel to the osteon (and hence MCF) axis. Since the mineral platelets are parallel to the loading $z$-direction, and zero mean stress is applied in the direction perpendicular to the $z$-axis, the normal stress in the $x-y$ plane would vanish if this were a homogeneous material. However, confinement associated with heterogeneity introduces large stress concentration in the gap region between mineral platelets in the $z$-direction. Figure 2 shows the distribution of hydrostatic stress in the VE subjected to uniaxial tension.

The mechanism leading to the observed stress concentration is the confinement of the softer phase by the hard mineral platelets. The platelets are staggered in the $z$-direction forming gaps between them. These gaps are stochastically placed

in the $z$-direction, and hence, the probability that they align in the $x-y$ plane is small. Hence, most gaps are surrounded by neighboring mineral platelets, and their deformation is restricted by the surrounding hard phase. This greatly increases the hydrostatic stress in the gap regions. Figure 3a shows the probability distribution function (PDF) of the hydrostatic stress in the model of Fig. 2 subjected to a uniaxial applied strain of $\varepsilon_{zz}^\infty = 3 \times 10^{-3}$. The distribution is bimodal. The mean of the large peak in the vicinity of the origin is 2.2 MPa and corresponds to the hydrostatic stress computed based on the applied far-field strain. A secondary peak of mean 51.4 MPa appears. This corresponds to the hydrostatic stress in the inter-platelet gap regions. Therefore, the confinement-induced stress concentration is substantial, with the local hydrostatic stresses being $\sim 25$ times larger than the far-field average.

To demonstrate that this stress concentration effect is associated with confinement, the Poisson ratio of the soft phase is varied and the mean of the large hydrostatic stress peak in the distribution of Fig. 3a is plotted versus the Poisson ratio in Fig. 3b. The concentration effect is highly sensitive to the Poisson ratio of the matrix material, as expected. In the following simulation, we assume a moderate estimate of the Poisson's ratio of 0.4. The effect discussed can be enhanced drastically as the material is brought closer to the incompressible state.

The stress concentration effect discussed here occurs in the gap between platelets in the $z$-direction and is largely independent of the relative orientation of the packs of platelets in the $x-y$ plane (Fig. 1). Therefore, other mineral arrangement
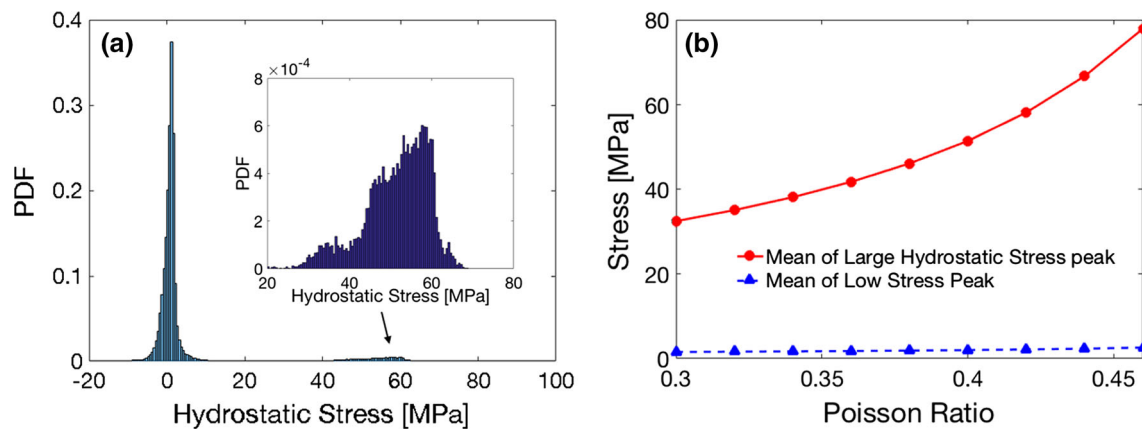
**Fig. 3** **a** Probability distribution function (based on the number of elements subjected to given stress) of the hydrostatic stress in the model subjected to a far-field strain of $3 \times 10^{-3}$. The matrix stiffness in this analysis is 1 GPa (Gupta et al. 2004; Meyers et al. 2008), and a value of 0.4 is selected for the Poisson ratio of the soft phase. The inset shows a detail of the large hydrostatic stress peak; **b** variation of the mean of the large hydrostatic stress peak in **a** with the Poisson ratio of the soft phase (red line and circles). The mean of the low stress peak is also shown (blue line and triangles); this value is constant since the imposed far field uniquely defines it

configurations should lead to the same stress concentration in the inter-platelet gaps. It is, however, noteworthy that the nanostructure varies between different bone types and different development stages (Reznikov et al. 2014). Randomly oriented MCFs have been reported in woven bone (Su et al. 2003) and during early stages callus formation where bone formation occurs rapidly to provide support to a healing fracture. Also, mineralized collagen fibrils with exclusively intra-fibrillar mineral (Nudelman et al. 2010) or with partial extra-fibrillar mineralization (Deshpande and Beniash 2008; Karunaratne et al. 2012) are reported under specific in vitro culture conditions. The current study does not attempt to capture such situations.

## 3.2 Energy released associated with interface NCP denaturation under uniaxial loading

The large stresses discussed in the previous section will result in interfacial NCP denaturation. The conditions under which this takes place and the energy released associated with this process are analyzed in this section. The stress-induced protein denaturation discussed here is essentially different from the sacrificial bonds proposed by Fantner et al., which related to separation and reforming of glue filaments involving van der Waals interactions (Fantner et al. 2005). The stress-induced protein denaturation (or dilatational bands) is defined by mechanical unfolding of NCPs at mineral–matrix interfaces, which is irreversible. Also, the sacrificial bonds are usually observed on fracture surfaces (Fantner et al. 2005), while the protein denaturation (dilatational bands) can occur even before microcrack propagation (Poundarik et al. 2012). To this end, the stress state at the scale of an inter-platelet gap, the size of the denaturation

front propagating at the interface between the mineral and organic phases, and the critical energy required to modify the interface need to be specified.

Figure 4 shows the normal stress distribution on the surface of a mineral platelet due to uniaxial far-field loading in the $z$-direction of the model in Fig. 2, with an imposed far-field strain of $\varepsilon_{zz}^{\infty} = 3 \times 10^{-3}$. The stress is generally small under uniaxial boundary condition, except in the gap region where it is tensile and large (red central region). An elliptical region is defined at the selected interface A (shown in Fig. 4b) and the nodes in this region are duplicated, effectively generating a small (closed) crack (shown edge-on in the inset to Fig. 4b). This feature represents a denatured region that opens upon the application of far-field loading.

The large normal stress acting at the interface will lead to the development of a denaturation front whose size depends on the stress distribution and the total strain energy available. We evaluate firstly the strain energy released, $U$, as the denaturation front grows at the interface under fixed far-field loading, $\varepsilon_{zz}^{\infty}$. To this end, we select a flaw size and solve the boundary value problem for given far-field condition with and without the flaw. The difference between the strain energy stored in these two states represents the energy released during the growth of the denaturation front up to the respective size. The procedure is repeated for various denaturation domain sizes and shapes. We assume full normal stress release within the region of denaturation and approximate the denaturation front shape with an ellipse having area $a$ and a ratio between the two semiaxis $R$. Figure 5 shows the distribution of normal stress acting at the interface for models with various values of the two parameters, $a$ and $R$, providing continuous snapshots during denaturation front propagation under large enough constant far-field loading.
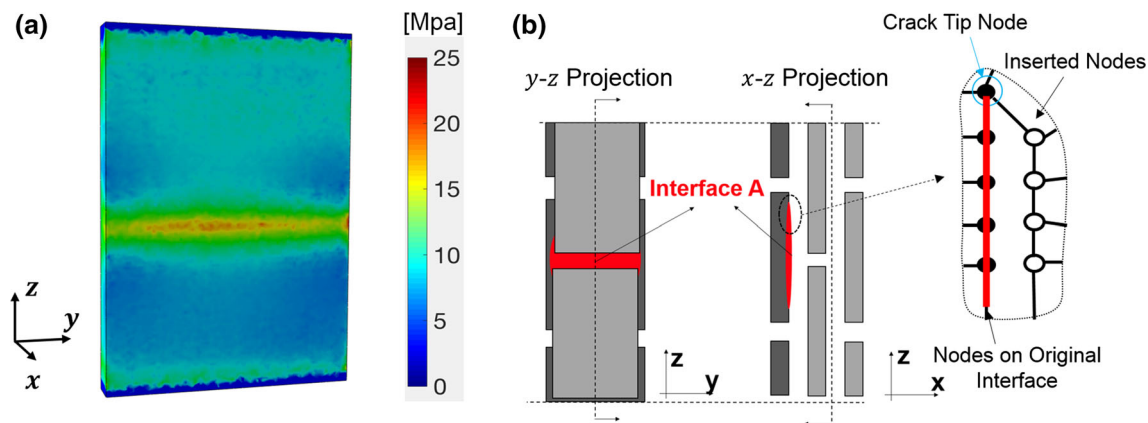
**Fig. 4** **a** Normal stress distribution at interface $A$ between mineral platelet and the organic phase, associated with a uniaxial far-field loading of $\varepsilon_{zz}^{\infty} = 3 \times 10^{-3}$; **b** Two projections of the stack of extra-fibrillar mineral platelets with the generic interface of interest $A$ shown in red. The inset schematic diagram shows how the crack is modeled by inserting a new set of nodes
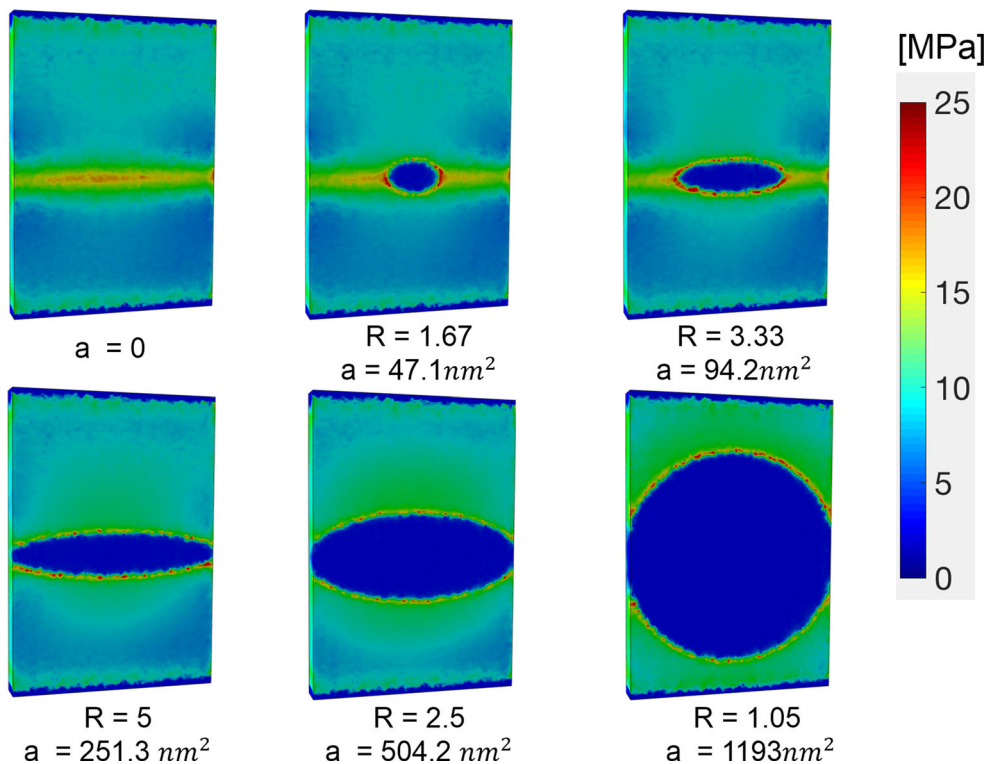


**Fig. 5** Normal stress distribution at the surface of a mineral platelet, with the denaturation domain shown by the central blue region. Configurations corresponding to multiple shapes and sizes of the denaturation domain are shown. The top line images show growth along the high stress region of the interface facing the gap, while the bottom line images show subsequent growth in the direction of the platelet length (or $z$-direction)

The strain energy released, $U$, upon the formation of an elliptical denaturation domain of semiaxis $m$ and $n$ ($m = \sqrt{Ra/\pi}$ and $n = \sqrt{a/R\pi}$) is shown in Fig. 6 as a function of parameter $a$. Curves for several values of $n$ are shown in Fig. 6. Under realistic growth conditions, the shape of the denaturation front evolves such that the stress intensity factor along the crack contour is constant and the energy release rate is maximized. These conditions correspond to the upper envelope of the curves in Fig. 6. The red dash curve shown in Fig. 6 is the physically relevant relation between the strain energy released and denaturation area.

The strain energy release rate, computed based on the data in Fig. 6 ($\partial U/\partial a$ or the tangent to the red line in Fig. 6), can be compared with the energy cost to produce denatura-
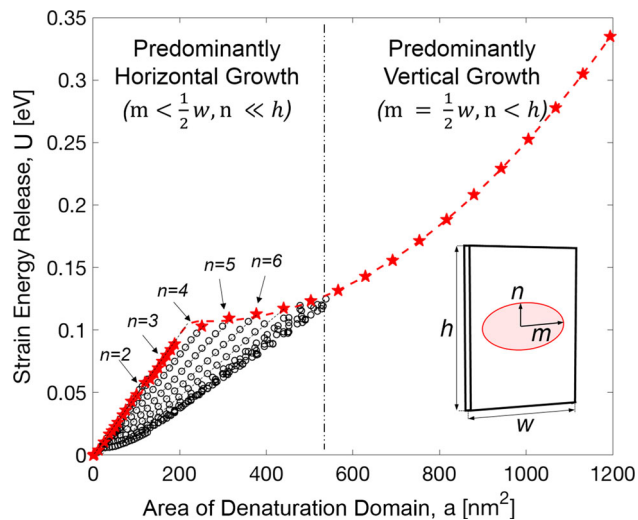
**Fig. 6** Variation of the strain energy released in the process of denaturation front growth from zero to given area, $a$. Numerical data obtained with the model in Fig. 2 are presented for various values of the semi-axis $n$ and area, $a$ (open circles). The red curve is the upper envelope of all numerical results and corresponds to the flaw shape that leads to the maximum energy released for given $a$. It represents the physically relevant energy release–denaturation area relation. The data correspond to a far field strain of $\varepsilon_{zz}^{\infty} = 3 \times 10^{-3}$

tion. Poundarik et al. (2012) suggested that each dilatational band complex comprises one OPN, which connects to the mineral and collagen via two OC molecules. The energy dissipation per dilatational band is estimated to range from 1.1 to 54.5 eV (Gupta et al. 2006; Poundarik et al. 2012). In view of this uncertainty, we consider a broad range of critical energy release rates $G_c$ and assume that NCPs are uniformly distributed at the interface associated with dilatational bands formation, and the area corresponding to one dilatational band ranges from 800 to 4000 nm² (McNally et al. 2012; Poundarik et al. 2012). Therefore, the upper bound $G_c^{upper} = 10.91$ mJ/m² (0.068 eV/nm².) is obtained by dividing the maximum value of the energy dissipation by the minimum area, and the lower bound $G_c^{lower} = 0.04$ mJ/m² ($2.5 \times 10^{-4}$ eV/nm²) is obtained by using the minimum value of the energy dissipation and the maximum area. Another data set, based on the measurement of the energy required to deform in tension an OPN molecule bonded to a mica surface using the tip of an AFM (Fantner et al. 2007), leads to an estimate of the critical energy (required to initiate denaturation) of 2.26 mJ/m², which is within the range mentioned above. To obtain this estimate from the respective data set (Fantner et al. 2007), we consider the work performed by the AFM cantilever up to the first minimum of the load–displacement curve and divide this quantity by the area of contact between the tip and the NCP film (reported to be 900 nm²).

It can be conceived that the debonding process is of a different nature than assumed here. Three types of interactions

have been discussed for mineral–organic interfaces in bone (Stock 2015): molecular entanglement, intermolecular interactions and mechanical interlocking. The macromolecular denaturation discussed here is the degradation under stress of an interface whose strength is derived primarily from molecular entanglements. The denaturation energy considered, based on the studies mentioned above (fracture energy release rate ranging from 0.04 mJ/m² to 10.91 mJ/m², is significantly smaller than that corresponding to an interface stabilized by electrostatic interactions ($\sim$ 200 mJ/m², (Ji 2008)) or hydrogen bonding (150 mJ/m², (Siegmund et al. 2008)). Hence, in case of competing mechanisms, the weakest link controls failure and the values considered here apply. Furthermore, the range considered is sufficiently broad to encompass other interface failure mechanisms and associated energies not envisioned here. The proposed general modeling methodology also applies when a larger interface toughness value is assumed (e.g., corresponding to hydrogen bonding). In this case, the size of the debonded region as well as the total energy released per unit volume of material would be smaller. With the strain energy release curve and critical energy release rate $G_c$, we can determine the size of the denaturation front corresponding to different far-field loadings. Different far-field strains $\varepsilon_{zz}^{\infty}$ correspond to different $U(a)$ curves. Since the problem is linear elastic, the maximum energy released (red curve in Fig. 6) scales with the square of the far-field strain. Figure 7 shows energy release curves similar to that in Fig. 6 for two ranges of far-field strains: $\varepsilon_{zz}^{\infty} = 1.5 \times 10^{-3}$ to $\varepsilon_{zz}^{\infty} = 3.8 \times 10^{-3}$ in Fig. 7a, and $\varepsilon_{zz}^{\infty} = 25 \times 10^{-3}$ to $\varepsilon_{zz}^{\infty} = 65 \times 10^{-3}$ in Fig. 7b. The first range overlaps with physiological conditions, while the second represents situations in the vicinity of stress concentrators. The solid red lines are described by the equation $G_c a$ and correspond to the lower and upper limits of the range of critical energy release rates considered here, i.e., $G_c = 0.04$ mJ/m² (in Fig. 7a) and 10.91 mJ/m² (in Fig. 7b). Interface denaturation takes place in situations corresponding to $U(\varepsilon_{zz}^{\infty}, a)$ curves that intersect or lay above the critical energy release red lines. If the $U(\varepsilon_{zz}^{\infty}, a)$ curve intersects the red line, denaturation is initiated but stops before extending to the entire interface of the respective platelet. Full interface denaturation occurs when $U(\varepsilon_{zz}^{\infty}, a)$ is strictly above the respective red line. For example, for the weak interface corresponding to lower bound of the $G_c$ range, $G_c^{lower} = 0.04$ mJ/m²($2.5 \times 10^{-4}$ eV/nm²) (Fig. 7a), finite size denaturation is expected for far-field loads in the range $\varepsilon_{zz}^{\infty} = 2.15 \times 10^{-3}$ to $\varepsilon_{zz}^{\infty} = 3.15 \times 10^{-3}$, while for larger far fields the entire platelet interface denatured. For strong interface corresponding to $G_c^{upper} = 10.91$ mJ/m² (0.068 eV/nm²) (Fig. 7b), denaturation begins once the far-field strain becomes larger than $\varepsilon_{zz}^{\infty} = 35 \times 10^{-3}$. This is summarized in Eq. (1), in which $E_{dd}$ is the energy dissipated via this mechanism at given denaturation sites, $a$ is the
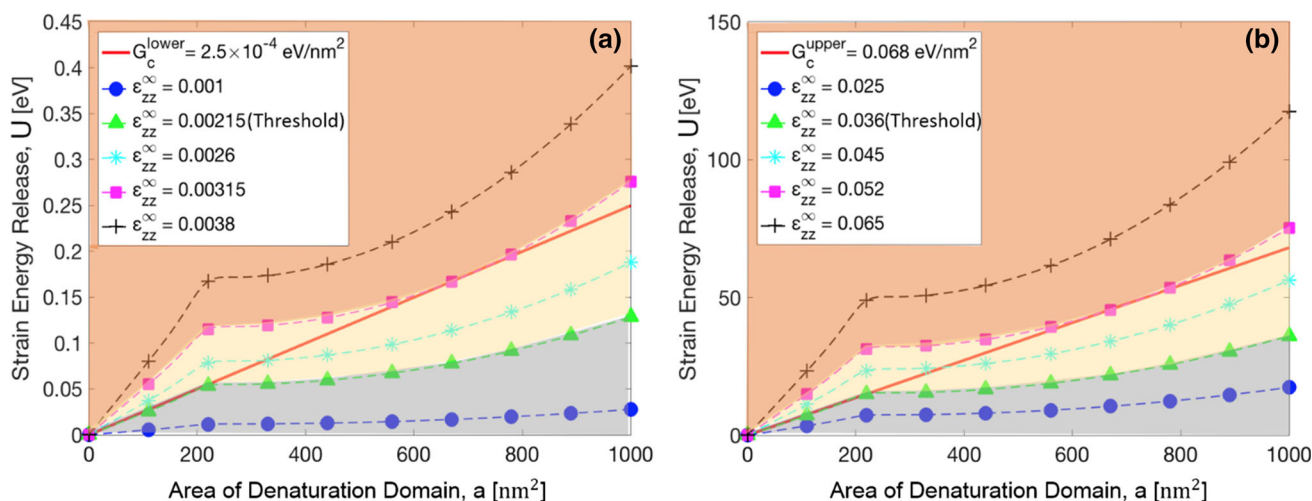
**Fig. 7** Strain energy released versus denaturation domain area corresponding to various far-field loading strains. The red solid lines represent the critical energy release required to produce interface denaturation. The red curve in **a** corresponds to the lower limit of the critical energy release per unit area of $G_c^{lower} = 0.04 \, \text{mJ/m}^2 (2.5 \times 10^{-4} \, \text{eV/nm}^2)$, while the red curve in **b** corresponds to the upper limit

of $G_c^{upper} = 10.91 \, \text{mJ/m}^2$ (0.068 eV/nm²). The bottom shaded area (gray) indicates far-field strain $\varepsilon_{zz}^\infty$ that do not lead to interface denaturation, the middle shaded area (yellow) indicates far-field strain $\varepsilon_{zz}^\infty$ that lead to finite size interface denaturation, while the top shaded area (orange) indicates far-field strains $\varepsilon_{zz}^\infty$ that lead to full interface denaturation

current area of the denaturation domain and $A$ is the entire interfacial area:

$$E_{dd} = \begin{cases} 0, & U\left(\varepsilon_{zz}^\infty, a\right) < G_c a \text{ for all } a \\ G_c a, & \text{other} \\ G_c A, & U\left(\varepsilon_{zz}^\infty, a\right) > G_c a \text{ for all } a \end{cases} \quad (1)$$

Note that the far-field strain leading to full interface denaturation varies with the interface size. However, the threshold far-field strain at which denaturation happens first (the green triangles curve in Fig. 7) is independent of the interface configuration. The average energy dissipated by each denaturation sites $E_{dd}$ can be evaluated as 1.1 eV and 54.5 eV for weak and strong interfaces, respectively.

Based on the strain in Fig. 7a, it can be concluded that for the physiological strain of $3 \times 10^{-3}$ the denaturation region is smaller than 500 nm², and the energy released is negligible, on the order of 0.1 eV. However, as has been already reported (Cowin and Weinbaum 1998; Rath Bonivtch et al. 2007), bone experiences strain amplification at stress concentrators such as macroscale crack tips, microcracks, and osteocyte lacunae. Thus, dilatational bands are expected in the vicinity of these stress concentrators. This is in general agreement with experimental observations (Vashishth et al. 2000; Poundarik et al. 2015) and indicates that the mechanism contributes to toughening. In order to calculate the overall toughness enhancement associated with this mechanism, we discuss in the next section the energy dissipation associated with dilatational bands in the vicinity of a macroscale crack tip stress concentrator.

## 3.3 Estimation of the toughening contribution of the proposed mechanism

In this section, we consider a crack defined in the $X$–$Y$ plane of Fig. 8, growing in the direction transverse to osteons and loaded in Mode I with a far field leading to a stress intensity factor $K_I$. The material is transversely isotropic with the Z-direction being the axis normal to the plane of isotropy. The coordinate system indicated by capitals is tied to the macroscopic crack tip. The experimental elastic constants (Dong and Guo 2004) expressed in the coordinate system of Fig. 8 are: $E_Z = 16.61 \, \text{GPa}$, $E_X = 9.55 \, \text{GPa}$, $G_{XY} = 3.28 \, \text{GPa}$, $v_{XZ} = 0.37$, $v_{XY} = 0.45$. The asymptotic stress field in the vicinity of the tip is given by (Sih et al. 1965):

$$\sigma_{XX} = \frac{K_I}{\sqrt{(2r)}} \text{Re} \left[ \frac{\mu_1 \mu_2}{\mu_1 - \mu_2} \left( \frac{\mu_2}{\sqrt{\cos\theta + \mu_2 \sin\theta}} - \frac{\mu_1}{\sqrt{\cos\theta + \mu_1 \sin\theta}} \right) \right]$$

$$\sigma_{ZZ} = \frac{K_I}{\sqrt{(2r)}} \text{Re} \left[ \frac{\mu_1 \mu_2}{\mu_1 - \mu_2} \left( \frac{\mu_1}{\sqrt{\cos\theta + \mu_2 \sin\theta}} - \frac{\mu_2}{\sqrt{\cos\theta + \mu_1 \sin\theta}} \right) \right]$$

$$\tau_{XZ} = \frac{K_I}{\sqrt{(2r)}} \text{Re} \left[ \frac{\mu_1 \mu_2}{\mu_1 - \mu_2} \left( \frac{1}{\sqrt{\cos\theta + \mu_1 \sin\theta}} - \frac{1}{\sqrt{\cos\theta + \mu_2 \sin\theta}} \right) \right] \quad (2)$$
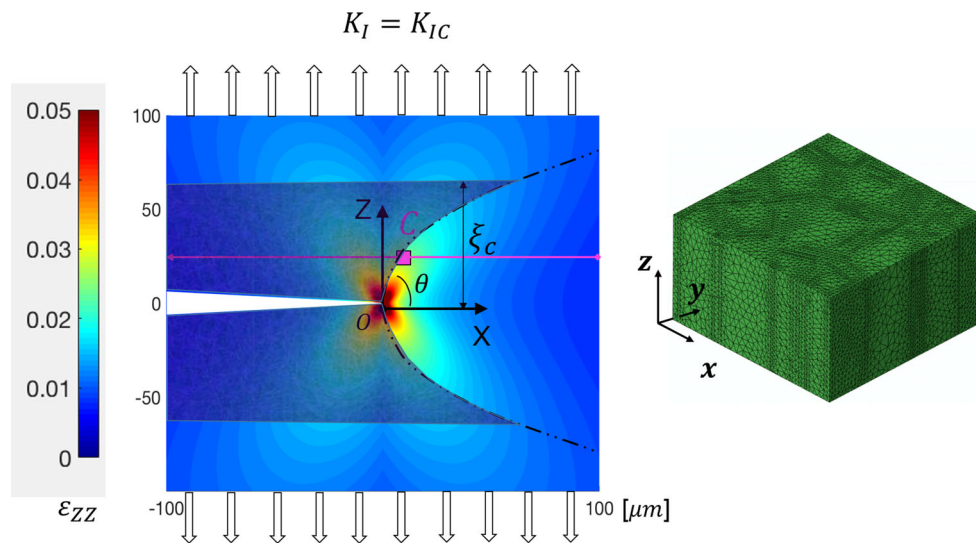
**Fig. 8** Schematic diagram shows the loading of volume elements in the field of a major crack. The coordinate system $(X, Y, Z)$ is tied to the crack tip, while $(x, y, z)$ is tied to the VE defined at point C. The color map shows the strain field $\varepsilon_{ZZ}$ in the vicinity of the tip and related to the stress field of Eq. (2). Point C represents the point along the path followed by the VE (magenta line) at which the VE experiences the critical denaturation conditions. The distance from point C to the crack plane is denoted by $\xi$. The dash-dot black line represents the locus of points C at various distances $\xi$, which is shown in Fig. 9a. Parameter $\xi_c$ represents the critical value of $\xi$ above which no denaturation is expected. Therefore, the darker blue, shaded region parallel to the crack plane indicates the DWZ

where $\theta$ is the angle made by the position vector of length r with the plane of the crack (with the x-direction), and $\mu_1, \mu_2$ are the roots with positive imaginary part from two pairs of complex conjugate roots of the reduced sextic equation (Stroh 1962):

$$c_{11}\mu^4 - 2c_{16}\mu^3 + (2c_{12} + c_{66})\mu^2 t - 2*c_{26}\mu + c_{22} = 0 \quad (3)$$

and $c_{ij}$ are entries in the reduced stiffness matrix. For current setup, the two root are $\mu_1 = 0.2066 + 0.8163\,i$, $\mu_2 = -0.2066 + 0.8163\,i$. (The detailed calculation is presented in supplementary information).

Consider crack growth conditions defined macroscopically by $K_I = K_{Ic}$, where $K_{IC}$ is the intrinsic crack initiation toughness of bone reported as $1.5\,\text{MPa}\sqrt{\text{m}}$ (Mullins et al. 2007). In the vicinity of the crack tip, we can define a region in which NCPs denaturation mechanism operates. Here, we denote this region as denaturation wake zone (DWZ). The objective of this section is to estimate the location and size of DWZ and the overall contribution of this denaturation mechanism to toughness. This discussion can be applied to both macro- and microcracks.

To estimate the size and position of DWZ, we consider the loading history of an infinitesimal volume of material C (shown schematically by the magenta square in Fig. 8) located at a distance $\xi$ from the plane of the crack, during crack growth. Due to the scale separation between the nanoscale models in Fig. 2 and that at which the crack is defined, we envision that the 'infinitesimal' volume element

discussed here is identical to the volume element considered in the discussion of the mechanism in the previous section. This volume element C is loaded by a stress field (associated with the crack tip) of increasing amplitude as it approaches the crack tip, after which the field decreases, as the respective location moves into the wake of the crack. The level of denaturation corresponds to the largest stress conditions experienced by the volume element along the magenta path shown in Fig. 8 (here, instead of moving the crack tip, we tie the coordinate system to the tip and observe the motion of the volume element of interest in this frame).

To identify the maximum loading state along the magenta path in Fig. 8 (denoted by point C), it is necessary to specify the combination of stress components related to the denaturation mechanism discussed above. A material point in the crack tip region is loaded in a complex way. The normal strain $\varepsilon_{zz}^\infty$ applied to the volume element in the previous section is identical to the normal strain $\varepsilon_{ZZ}$ produced by the crack at the location of interest. In addition, other strain components are present in the crack tip field and should be considered as far-field loads for the VE, as shown in Eq. (2). The normal stress on the mineral–organic interfaces of the volume element has two components: the far-field stress $\sigma_{xx}$ and the normal stress resulting from confinement and associated with $\sigma_{zz}^\infty$ (Sect. 3.1). While the distribution of the second component along a mineral plate is non-uniform, see Fig. 4, the far-field normal stress $\sigma_{xx}$ has a constant value over the same area. If tensile, $\sigma_{xx}$ can drive interface denaturation without
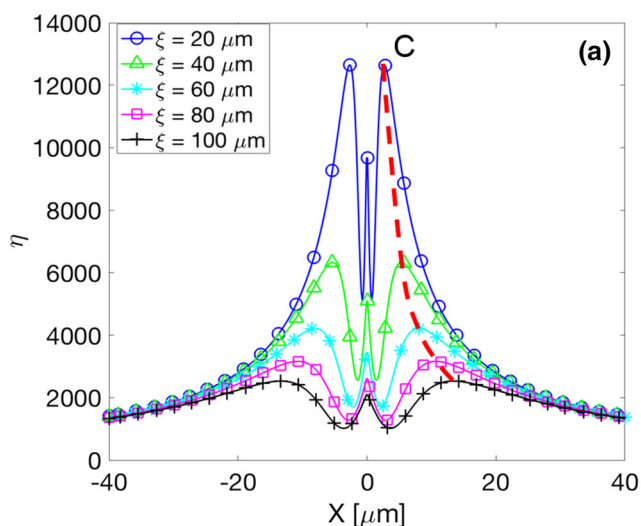
**Fig. 9** **a** Variation of the loading parameter $\eta$ with position X along paths parallel to the crack plane and located at distance $\xi$ from the crack. The maximum along each of these curves represents the position at which the nanoscale VE experiences the largest loading conditions along the respective path. The dashed red line marks the position of the peaks and corresponds to the dash-dot black line in Fig. 8; **b** Strain energy release curves, $G(a)$, for various values of the angle $\alpha$ between the X and $x$-axis in Fig. 8 for a material point C located at $\xi = 10\,\mu\text{m}$, $50\,\mu\text{m}$ and $100\,\mu\text{m}$ from the crack plane

the contribution of the mechanism relying on confinement. In situations where this condition is fulfilled, we consider that the interface opens fully, i.e., over the entire surface of the mineral platelet. We adopt the fracture mechanics view in which the relevant parameter describing the mixed mode loading of the interface is $\eta = \sqrt{\sigma_{xx}^2 + \tau_{xz}^2}$. Figure 9a shows the variation of parameter $\eta$ along paths parallel to the crack in Fig. 8 and at various distances from it, $\xi$. These curves exhibit a peak at a position X relative to the tip O, which depends on distance $\xi$ of the material point from the crack plane. As the distance $\xi$ increases, parameter $\eta$ decreases. This is shown by the dashed red line in Fig. 9a and by the black dash-dot line in Fig. 8. This is the locus of points in the crack tip region at which the nanoscale volume elements experience the critical load leading to the largest level of denaturation. Hence, we can find a critical distance $\xi_c$, above which no interface protein denaturation happened. Therefore, the DWZ can be defined as region parallel to the crack and behind the black dash line in Fig. 8 (shown by a darker shade of blue).

The analysis is further complicated by the fact that the volume element, which has its platelet longitudinal direction (the $z$-axis in Fig. 8) aligned with the osteons direction running perpendicular to the crack plane (Z-direction), can be nevertheless rotated about the $z$-axis with an arbitrary angle. Denote by $\alpha$ the angle between the X and $x$ axes. Therefore, it is necessary to identify the element orientation leading to the largest level of denaturation for each position of the element relative to the crack tip. In the case discussed in the previous section, the orientation of the volume element in
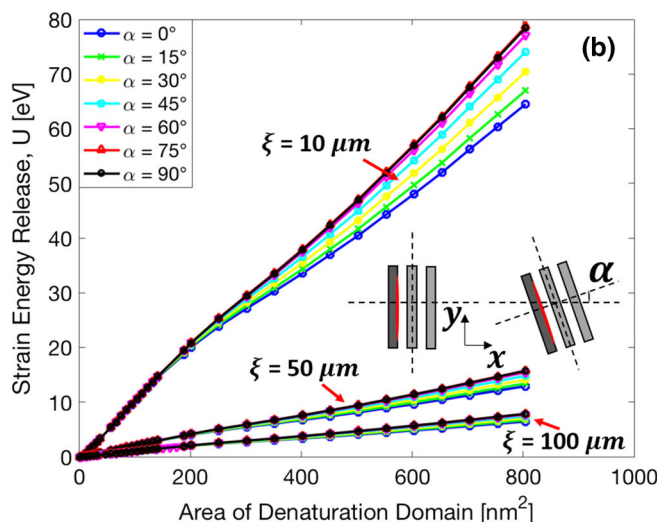
Fig. 1, relative to the $z$-axis, is irrelevant since the far-field load is uniaxial. In the crack tip case, the interface normal and shear stress components change as the interface rotates about the $z$-axis.

The analysis described in uniaxial loading condition, which leads to the strain energy release curves in Figs. 6 and 7, was repeated for multiple angles $\alpha$. Figure 9b shows the influence of the rotation angle $\alpha$ on the computed strain energy released $G(a)$. The data shown in the figure correspond to points C along the black dash-dot curve in Fig. 8 located at $\xi = 10\,\mu\text{m}$, $50\,\mu\text{m}$ and $100\,\mu\text{m}$ from the crack plane and to a crack loading defined by $K_I = 1.5\,\text{MPa}\sqrt{\text{m}}$. It is observed that $\alpha$ has a weak influence on $G(a)$. Therefore, we consider the average curve of the set shown in Fig. 9b to be representative for all orientations of the nanoscale volume element at the respective point in the crack tip field. We observe further that finite size denaturation is an exception under these conditions, and hence, in most cases, the full interface denaturation can be considered. This conclusion is consistent with confocal microscopy observations that all dilatational bands are of similar size, on the order of 100 nm (Poundarik et al. 2012).

With this information, we are in the position to evaluate the thickness of DWZ, which experiences denaturation during crack growth. The critical thickness of DWZ, $\xi_c$, depends on the critical denaturation conditions determined in the section and on the crack tip field analysis presented in this section. This fracture process zone is shown as shaded (darker blue) band in Fig. 8. For $K_I = 1.5\,\text{MPa}\sqrt{\text{m}}$ corresponding to macroscopic critical crack growth conditions and the range

of $G_c$ considered in the previous section ($G_c^{\text{lower}} < G_c < G_c^{\text{upper}}$), the thickness of DWZ around the crack $\xi_c$ can range from 15 $\mu$m (for $G_c^{\text{upper}}$) to 1.1 mm (for $G_c^{\text{lower}}$).

Further, we evaluate the overall contribution of this stress-induced NCP denaturation mechanism to microcrack toughness. To this end, we integrate the energy dissipated in the entire crack tip region corresponding to unit crack advance along the crack front. The associated contribution to the energy release rate results

$$\Delta G_{dd} = E_{dd}\rho\left(2\xi_c\right), \qquad (4)$$

where $E_{dd}$ is the energy dissipated per denaturation sites computed in the previous section, $\rho$ is the average density of denaturation sites in the crack tip affected region estimated from extra-fibrillar mineral arrangement in Fig. 1b. Here, $\rho = 1.29 \times 10^4/\mu\text{m}^3$ (see detailed calculation in supplementary information). $\xi_c$ is the critical thickness of DWZ evaluated above. As reported by Poundarik et al. (2012), the NCPs are spatially distributed in bone matrix. Microdissection of $14 \times 10^5 \mu m^3$ human cortical bone (Sroga and Vashishth 2012) shows $\sim 25$ times more OC is in the diffuse damaged regions containing dilatational bands ($8.05 \pm 1.71$ nmol OC/g bone) than in the adjacent non-damaged control. OPN content in the damaged area ($0.63 \pm 0.14$ nmol OPN/g bone) is also higher than in its non-damaged control. Assuming the bone density is 1.9 g/cm$^3$, the OC concentration in the diffuse damaged regions is $9.21 \pm 1.95 \times 10^3/\mu\text{m}^3$ and OPN concentration can be $7.21 \pm 1.60 \times 10^2/\mu\text{m}^3$. Considering OC accounts for 15–25% of the total protein (Hall 2015), the total concentration of the NCPs of interest should range from $3.68 \times 10^4$ to $6.14 \times 10^4/\mu\text{m}^3$, which is on the same order of magnitude with the estimated denaturation sites density $\rho = 1.29 \times 10^4/\mu\text{m}^3$. Therefore, the contribution to the overall toughness is estimated for the specified range of $\xi_c$ as $\Delta G_{dd} = 3.38\,\text{J/m}^2$ to $5.00\,\text{J/m}^2$ for weak and strong interfaces, respectively. The corresponding enhancement of the apparent stress intensity factor is $\Delta K_{dd} = 0.272$ and $0.331\,\text{MPa}\sqrt{\text{m}}$ (in plane stress condition, see the detailed calculation in supplementary information). Considering the baseline critical stress intensity factor, $K_{IC} = 1.5\,\text{MPa}\sqrt{\text{m}}$, the overall toughening effect from this toughening mechanism is evaluated to range from 18 to 22%.

Equation (4) indicates that the energy dissipation scales linearly with the critical thickness $\xi_c$ of the DWZ. Also, from Eq. (2), it is seen that the critical thickness $\xi_c$ scales quadratically with the intrinsic toughness $K_{IC}$. Hence, the toughening effect scales with the square of the toughness $K_{IC}$. In case of a macroscopic crack, $K_{IC}$ increases with as the crack grows as described by the R-curve of bone fracture toughness (Vashishth 2004). Also, there is additional energy dissipation from microcracks in the vicinity of the macroscopic crack. Therefore, we expect the mechanism discussed here to contribute more than 22% to the overall toughness of bone. It is interesting to compare this estimation to the variation of the toughness of bone between wild type and genetically modified mice (CO and OPN knockouts), which was reported to be 31% (Poundarik et al. 2012). Dilatational bands are not reported in the knockouts due to the absence of the relevant NCPs, which inhibits the operation of the toughening mechanism discussed here. Considering the uncertainties involving the interfacial behavior of mineral/mineral interface, the agreement with this experimental result provides support to the analysis presented.

## 4 Conclusion

The fundamental understanding of fracture behavior of bone relies on a thorough understanding of the behavior of energy dissipation at multiple length scales. This article explores a stress-induced nanoscale mechanism leading to the formation of dilatational bands. The mechanism is based on the observation that the extra-fibrillar mineral arrangement and, in particular, the confinement imposed on the organic phase by the mineral, lead to large hydrostatic stress concentration and significant stress field spatial fluctuations at the nanoscale. These large local stresses support NCPs denaturation without the creation of physical cracks, but with associated energy dissipation. Conditions in which this mechanism operates at the nanoscale are evaluated using a model that takes into account the details of the bone architecture at the respective scale. The model leads to the conclusion that denaturation is to be expected only in the vicinity of stress concentrators in bone, i.e., in the vicinity of microscale/macroscale sites, where the strain field is larger than the mean field associated with physiological conditions. Further, the toughening contribution of this mechanism is evaluated by exploring how nanoscale denaturation takes place in the vicinity of a major crack tip. It is found that a region (DWZ), in the vicinity of the tip where denaturation is expected, is confined within the critical distance $\xi_c$ parallel to the crack. Also, full interface denaturation is expected within the majority DWZ region. Finally, the estimations of the energy dissipation and the size of DWZ allow concluding that the mechanism increases the toughness of bone on the order of 20% and will increase with crack length contribute to the rising R-curve behavior observed in bone (Vashishth et al. 1997). The current model gives fundamental mechanical understand for the formation of dilatational bands and decent estimation of toughening effect from the stress-induced toughening mechanism in bone.

## Compliance with ethical standard

## References

Almer JD, Stock SR (2005) Internal strains and stresses measured in cortical bone via high-energy X-ray diffraction. J Struct Biol 152:14–27

Almer JD, Stock SR (2007) Micromechanical response of mineral and collagen phases in bone. J Struct Biol 157:365–370. https://doi.org/10.1016/j.jsb.2006.09.001

Alexander B, Daulton TL, Genin GM et al (2012) The nanometre-scale physiology of bone: steric modelling and scanning transmission electron microscopy of collagen–mineral structure. J R Soc Interface 9:1774–1786. https://doi.org/10.1098/rsif.2011.0880

Bonar LC, Lees S, Mook HA (1985) Neutron diffraction studies of collagen in fully mineralized bone. J Mol Biol 181:265–270

Boskey AL, Gadaleta S, Gundberg C et al (1998) Fourier transform infrared microspectroscopic analysis of bones of osteocalcin-deficient mice provides insight into the function of osteocalcin. Bone 23:187–196. https://doi.org/10.1016/S8756-3282(98)00092-1

Burger C, Zhou H-W, Wang H et al (2008) Lateral packing of mineral crystals in bone collagen fibrils. Biophys J 95:1985–1992. https://doi.org/10.1529/biophysj.107.128355

Burr DB, Milgrom C, Fyhrie D et al (1996) In vivo measurement of human tibial strains during vigorous activity. Bone 18:405–410. https://doi.org/10.1016/8756-3282(96)00028-2

Burr DB, Turner CH, Naick P et al (1998) Does microdamage accumulation affect the mechanical properties of bone? J Biomech 31:337–345. https://doi.org/10.1016/S0021-9290(98)00016-5

Ciuchi IV, Olariu CS, Mitoseriu L (2013) Determination of bone mineral volume fraction using impedance analysis and Bruggeman model. Mater Sci Eng B 178:1296–1302. https://doi.org/10.1016/j.mseb.2013.04.001

Cowin SC, Weinbaum S (1998) Strain amplification in the bone mechanosensory system. Am J Med Sci 316:184–188. https://doi.org/10.1016/S0002-9629(15)40399-4

De Buffrénil V, Dabin W, Zylberberg L (2004) Histology and growth of the cetacean petro-tympanic bone complex. J Zool 262:371–381. https://doi.org/10.1017/S0952836903004758

Deshpande AS, Beniash E (2008) Bioinspired synthesis of mineralized collagen fibrils. Cryst Growth Des 8:3084–3090. https://doi.org/10.1021/cg800252f

Ellman R, Spatz J, Cloutier A et al (2013) Partial reductions in mechanical loading yield proportional changes in bone density, bone architecture, and muscle mass. J Bone Miner Res 28:875–885. https://doi.org/10.1002/jbmr.1814

Fantner GE, Hassenkam T, Kindt JH et al (2005) Sacrificial bonds and hidden length dissipate energy as mineralized fibrils separate during bone fracture. Nat Mater 4:nmat1428–616. https://doi.org/10.1038/nmat1428

Fantner GE, Adams J, Turner P et al (2007) Nanoscale ion mediated networks in bone: osteopontin can repeatedly dissipate large amounts of energy. Nano Lett 7:2491–2498. https://doi.org/10.1021/nl0712769

Fratzl P, Paris O, Klaushofer K, LW J (1996) Bone mineralization in an osteogenesis imperfecta mouse model studied by small-angle X-ray scattering. J Clin Invest 97(2):396–402. https://doi.org/10.1172/JCI118428

Grynpas MD, Bonar LC, Glimcher MJ (1984) X-ray diffraction radial distribution function studies on bone mineral and synthetic cal-cium phosphates. J Mater Sci 19:723–736. https://doi.org/10.1007/BF00540442

Gupta HS, Messmer P, Roschger P et al (2004) Synchrotron diffraction study of deformation mechanisms in mineralized tendon. Phys Rev Lett 93:158101. https://doi.org/10.1103/PhysRevLett.93.158101

Gupta HS, Fratzl P, Kerschnitzki M et al (2006) Evidence for an elementary process in bone plasticity with an activation enthalpy of 1 ev. J R Soc Interface 4:277–282. https://doi.org/10.1098/rsif.2006.0172

Hall BK (2015) Chapter 24—Osteoblast and osteocyte diversity and osteogenesis in vitro. Bones and cartilage, 2nd edn. Academic, San Diego, pp 401–413

Hamed E, Lee Y, Jasiuk I (2010) Multiscale modeling of elastic properties of cortical bone. Acta Mech 213:131–154. https://doi.org/10.1007/s00707-010-0326-5

Hamed E, Jasiuk I, Yoo A et al (2012) Multi-scale modelling of elastic moduli of trabecular bone. J R Soc Interface 9:1654–1673. https://doi.org/10.1098/rsif.2011.0814

Hang F, Barber AH (2011) Nano-mechanical properties of individual mineralized collagen fibrils from bone tissue. J R Soc Interface 8:500–505. https://doi.org/10.1098/rsif.2010.0413

Hang F, Gupta HS, Barber AH (2014) Nanointerfacial strength between non-collagenous protein and collagen fibrils in antler bone. J R Soc Interface 11:20130993

Hauschka PV, Wians FH (1989) Osteocalcin-hydroxyapatite interaction in the extracellular organic matrix of bone. Anat Rec 224:180–188. https://doi.org/10.1002/ar.1092240208

Hodge AJ, Petruska JA (1962) Some recent results on the electron microscopy of tropocollagen structures. In: Breese SS Jr (ed) Proc. of the fifth Internat. Congr. for Electron Microscopy, vol 2. Academic, New York, p QQ-1

Jäger I, Fratzl P (2000) Mineralized collagen fibrils: a mechanical model with a staggered arrangement of mineral particles. Biophys J 79:1737–1746. https://doi.org/10.1016/S0006-3495(00)76426-5

Jaschouz D, Paris O, Roschger P et al (2003) Pole figure analysis of mineral nanoparticle orientation in individual trabecular of human vertebral bone. J Appl Cryst 36:494–498. https://doi.org/10.1107/S0021889803000566

Ji B (2008) A study of the interface strength between protein and mineral in biological materials. J Biomech 41:259–266. https://doi.org/10.1016/j.jbiomech.2007.09.022

Jin H, Lewis JL (2004) Determination of Poisson's ratio of articular cartilage by indentation using different-sized indenters. J Biomech Eng 126:138–145. https://doi.org/10.1115/1.1688772

Karunaratne A, Esapa CR, Hiller J et al (2012) Significant deterioration in nanomechanical quality occurs through incomplete extrafibrillar mineralization in rachitic bone: Evidence from in-situ synchrotron X-ray scattering and backscattered electron imaging. J Bone Miner Res 27:876–890. https://doi.org/10.1002/jbmr.1495

Kiviranta P, Rieppo J, Korhonen RK et al (2006) Collagen network primarily controls Poisson's ratio of bovine articular cartilage in compression. J Orthop Res 24:690–699. https://doi.org/10.1002/jor.20107

Koch CF, Johnson S, Kumar D et al (2007) Pulsed laser deposition of hydroxyapatite thin films. Mater Sci Eng C 27:484–494. https://doi.org/10.1016/j.msec.2006.05.025

Landis WJ, Hodgens KJ, Arena J et al (1996) Structural relations between collagen and mineral in bone as determined by high voltage electron microscopic tomography. Microsc Res Tech 33:192–202

Lees S, Prostak K (1988) The locus of mineral crystallites in bone. Connect Tissue Res 18:41–54. https://doi.org/10.3109/03008208809019071

Li X, Shephard MS, Beall MW (2005) 3D anisotropic mesh adaptation by mesh modification. Unstructured Mesh Generation. Com-

put Methods Appl Mech Eng 194:4915–4950. https://doi.org/10.1016/j.cma.2004.11.019

McNally EA, Schwarcz HP, Botton GA, Arsenault AL (2012) A model for the ultrastructure of bone based on electron microscopy of ion-milled sections. PLoS ONE 7(1):e29258. https://doi.org/10.1371/journal.pone.0029258

Meyers MA, Chen P-Y, Lin AY-M, Seki Y (2008) Biological materials: Structure and mechanical properties. Prog Mater Sci 53:1–206. https://doi.org/10.1016/j.pmatsci.2007.05.002

Mullins LP, Bruzzi MS, mchugh PE (2007) Measurement of the microstructural fracture toughness of cortical bone using indentation fracture. J Biomech 40:3285–3288. https://doi.org/10.1016/j.jbiomech.2007.04.020

Nair AK, Gautieri A, Chang SW, Buehler MJ (2013) Molecular mechanics of mineralized collagen fibrils in bone. Nat Commun 4:1724

Nair AK, Gautieri A, Buehler MJ (2014) Role of intrafibrillar collagen mineralization in defining the compressive properties of nascent bone. Biomacromolecules 15:2494–2500. https://doi.org/10.1021/bm5003416

Nalla RK, Kinney JH, Ritchie RO (2003) Mechanistic fracture criteria for the failure of human cortical bone. Nat Mater 2:164–168. https://doi.org/10.1038/nmat832

Neil Dong X, Edward Guo X (2004) The dependence of transversely isotropic elasticity of human femoral cortical bone on porosity. J Biomech 37:1281–1287. https://doi.org/10.1016/j.jbiomech.2003.12.011

Nikel O, Laurencin D, mccallum SA et al (2013) NMR investigation of the role of osteocalcin and osteopontin at the organic–inorganic interface in bone. Langmuir 29:13873–13882. https://doi.org/10.1021/la403203w

Peroos S, Du Z, de Leeuw NH (2006) A computer modelling study of the uptake, structure and distribution of carbonate defects in hydroxy-apatite. Biomaterials 27:2150–2161. https://doi.org/10.1016/j.biomaterials.2005.09.025

Pidaparti RM, Chandran A, Takano Y, Turner CH (1996) Bone mineral lies mainly outside collagen fibrils: predictions of a composite model for osternal bone. J Biomech 29:909–916

Poundarik AA, Gundberg CM, Vashishth D (2011) Non-collagenous proteins influence bone crystal size and morphology: a SAXS study. In: 2011 IEEE 37th annual northeast bioengineering conference (NEBEC), Troy, pp 1–2. https://doi.org/10.1109/nebc.2011.5778671

Poundarik AA, Diab T, Sroga GE et al (2012) Dilatational band formation in bone. Proc Natl Acad Sci. https://doi.org/10.1073/pnas.1201513109/-/dcsupplemental

Poundarik AA, Wu P-C, Evis Z et al (2015) A direct role of collagen glycation in bone fracture. J Mech Behav Biomed Mater 52:120–130. https://doi.org/10.1016/j.jmbbm.2015.08.012

Rath Bonivtch A, Bonewald LF, Nicolella DP (2007) Tissue strain amplification at the osteocyte lacuna: a microstructural finite element analysis. J Biomech 40:2199–2206. https://doi.org/10.1016/j.jbiomech.2006.10.040

Reznikov N, Shahar R, Weiner S (2014) Bone hierarchical structure in three dimensions. Acta Biomater 10:3815–3826. https://doi.org/10.1016/j.actbio.2014.05.024

Rho J-Y, Kuhn-Spearing L, Zioupos P (1998) Mechanical properties and the hierarchical structure of bone. Med Eng Phys 20:92–102. https://doi.org/10.1016/S1350-4533(98)00007-1

Ritter NM, Farach-Carson MC, Butler WT (1992) Evidence for the formation of a complex between osteopontin and osteocalcin. J Bone Miner Res 7:877–885. https://doi.org/10.1002/jbmr.5650070804

Rubin MA, Jasiuk I, Taylor J et al (2003) TEM analysis of the nanostructure of normal and osteoporotic human trabecular bone. Bone 33:270–282. https://doi.org/10.1016/S8756-3282(03)00194-7

Schaffler MB, Radin EL, Burr DB (1989) Mechanical and morphological effects of strain rate on fatigue of compact bone. Bone 10:207–214. https://doi.org/10.1016/8756-3282(89)90055-0

Schaffler MB, Choi K, Milgrom C (1995) Aging and matrix microdamage accumulation in human compact bone. Bone 17:521–525. https://doi.org/10.1016/8756-3282(95)00370-3

Schwarcz HP, mcnally EA, Botton GA (2014) Dark-field transmission electron microscopy of cortical bone reveals details of extrafibrillar crystals. J Struct Biol 188:240–248. https://doi.org/10.1016/j.jsb.2014.10.005

Seref-Ferlengez Z, Basta-Pljakic J (2014) Structural and mechanical repair of diffuse damage in cortical bone in vivo. J Bone Miner Res 29:2537–2544. https://doi.org/10.1002/jbmr.2309

Sih GC, Paris PC, Irwin GR (1965) On cracks in rectilinearly anisotropic bodies. Int J FractMech 1:189–203. https://doi.org/10.1007/BF00186854

Siegmund T, Allen MR, Burr DB (2008) Failure of mineralized collagen fibrils: modeling the role of collagen cross-linking. J Biomech 41:1427–1435. https://doi.org/10.1016/j.jbiomech.2008.02.017

Sroga GE, Vashishth D (2012) Effects of bone matrix proteins on fracture and fragility in osteoporosis. Curr Osteoporos Rep 10:141–150. https://doi.org/10.1007/s11914-012-0103-6

Stock SR (2015) The mineral–collagen interface in bone. Calcif Tissue Int 97:1–19. https://doi.org/10.1007/s00223-015-9984-6

Stroh AN (1962) Steady state problems in anisotropic elasticity. J Math Phys 41:77–103. https://doi.org/10.1002/sapm196241177

Su X, Sun K, Cui FZ, Landis WJ (2003) Organization of apatite crystals in human woven bone. Bone 32:150–162. https://doi.org/10.1016/S8756-3282(02)00945-6

Taylor D, Hazenberg JG, Lee TC (2007) Living with cracks: damage and repair in human bone. Nat Mater 6:263–268. https://doi.org/10.1038/nmat1866

Termine JD, Kleinman HK, Whitson SW et al (1981) Osteonectin, a bone-specific protein linking mineral to collagen. Cell 26:99–105. https://doi.org/10.1016/0092-8674(81)90037-4

Tresoldi I, Oliva F, Benvenuto M et al (2013) Tendon's ultrastructure. Muscles Ligaments Tendons J 3(1):2–6. https://doi.org/10.11138/mltj/2013.3.1.002

Vashishth D (2004) Rising crack-growth-resistance behavior in cortical bone: implications for toughness measurements. J Biomech 37:943–946. https://doi.org/10.1016/j.jbiomech.2003.11.003

Vashishth D, Behiri JC, Bonfield W (1997) Crack growth resistance in cortical bone: concept of microcrack toughening. J Biomech 30:763–769. https://doi.org/10.1016/S0021-9290(97)00029-8

Vashishth D, Koontz J, Qiu SJ et al (2000) In vivo diffuse damage in human vertebral trabecular bone. Bone 26:147–152. https://doi.org/10.1016/S8756-3282(99)00253-7

Weiner S, Traub W, Wagner HD (1999) Lamellar bone: structure–function relations. J Struct Biol 126:241–255. https://doi.org/10.1006/jsbi.1999.4107

Yuan F, Stock SR, Haeffner DR et al (2010) A new model to simulate the elastic properties of mineralized collagen fibril. Biomech Model Mechanobiol 10:147–160. https://doi.org/10.1007/s10237-010-0223-9

Zimmermann EA, Gludovatz B, Schaible E et al (2014) Fracture resistance of human cortical bone across multiple length-scales at physiological strain rates. Biomaterials 35:5472–5481. https://doi.org/10.1016/j.biomaterials.2014.03.066

Zioupos P, Currey JD (1998) Changes in the stiffness, strength, and toughness of human cortical bone with age. Bone 22:57–66. https://doi.org/10.1016/S8756-3282(97)00228-7